Article

Experimental Study of Proppant Placement Characteristics in Curving Fractures

Zhiying Wu, Chunfang Wu and Linbo Zhou *

State Key Laboratory of Shale Oil and Gas Enrichment Mechanisms and Effective Development,
Beijing 100101, China
* Correspondence: xiangao729@163.com

Abstract: Proppant placement in hydraulic fractures is crucial for avoiding fracture closure and maintaining a high conductivity pathway for oil and gas flow from the reservoir. The curving fracture is the primary fracture form in formation and affects proppant–fluid flow. This work experimentally examines proppant transport and placement in narrow curving channels. Four dimensionless numbers, including the bending angle, distance ratio, Reynolds number, and Shields number, are used to analyze particle placement in curving fractures. The results indicate that non-uniform proppant placement occurs in curving fractures due to the flow direction change and induces an irregular proppant dune. The dune height and covered area are lower than that in the straight fracture. The curving pathway hinders proppant distribution and leads to a dune closer to the inlet. When the distance increases between the inlet and curving section, a large depleted zone in the curving section will be formed and hinder oil and gas flowback. The covered area has negative linear correlations with the Reynolds number and Shields numbers. Four dimensionless parameters are used to develop a model to quantitatively predict the covered area of particle dune in curving fractures.

Keywords: hydraulic fracturing; proppant dune; proppant placement; complicated fracture; multiphase flow

1. Introduction

Hydraulic fracturing has become an essential method to create complex fractures in unconventional reservoirs to improve oil and gas recovery. Proppants should be transported by fracturing fluid into the fracture [1,2]. Sufficient proppants can avoid fracture closure and maintain a high conductivity pathway for liquid flowback from the reservoir. Many factors, including the fracture shape, injection parameters, and proppant properties, change particle placement [3–5]. Experimental results have proven that pre-existing cracks significantly affect hydraulic fracture propagation. The hydraulic fracture probably deviates into a pre-existing fracture during the intersection and then turns to the original direction. Typically, a hydraulic fracture is curved and irregular [6–10], and the complicated pathway probably affects particle–fluid flow, which changes particle distribution [11–13]. A specific understanding of proppant placement characteristics in a curving fracture with bends is crucial to optimizing fracturing design and enhancing the stimulation effect for unconventional reservoirs.

Various narrow channels were developed based on the similarity theory of fluid mechanics to study proppant placement in hydraulic fracture. For simplicity, vertical planar channels with narrow widths have been used to represent hydraulic fractures for decades. A straight channel containing two parallel acrylic panels was first set up by Kern et al. [14]. Sands and water were injected into the channel. It was observed that particle suspension and settling were two primary transport mechanisms in the straight fracture. An initial sand dune would form near the inlet due to particle settling. The injected sands flowed through the initial dune and deposited to the backside for the dune development toward the

fracture tip. The dune would be in equilibrium, and the subsequently injected sands were suspended deeper into the experimental channel. Babcock et al. [15] used a planar channel to study the sand buildup mechanisms. Tap water and three types of sand were employed in the experiment. It was found that the equilibrium bed height would significantly vary as the fluid velocity increases or decreases. A correlation equation was developed for the prediction of the equilibrium height and velocity related to the proppant type and size, the fluid properties, and the fracture geometry. According to the experimental channel at the STIM-LAB facilities, Wang et al. [16] developed a bi-power law model to calculate the equilibrium height. Water and low viscous fluid were used as fracturing fluids. The equation was widely used to model particle transport in vertical fracture and benchmark numerical simulation models [17–20]. Since particle settling would be reduced in the fracture with a small aperture, Zeng et al. [21] studied the particle dune shape in a super-narrow channel and developed two correlations to predict the dune height and coverage area. It was found that the dune in narrow fracture was higher than the wider one. Qu et al. [4] studied proppant placement in a wedge fracture. Low viscous fluid with 1.5 mPa·s was prepared as fracture fluid. The experimental channel with a contracted aperture was achieved by gradually inserting acrylic panels to gradually reduce the channel width. A regression model with four dimensionless parameters was proposed to predict the dune equilibrium height. Recently, other fracturing fluids, such as high viscosity guar gum, foamed fluid, and supercritical carbon dioxide, were tested in the straight channel to study proppant placement [5,22,23].

Because hydraulic fracturing can easily cause a complex fracture in the reservoir-developed fissures, complex experimental channels were developed to understand proppant placement in complicated fracture systems. Two types of channel systems have been proposed so far. A planar channel has several secondary and tertiary channels [13,24,25]. Sahai et al. [25] first developed a complex channel that contained a primary channel, three secondary channels, and two tertiary channels. The location of the subsidiary channels from the inlet impacted the proppant-covered area. It was found that the closest subsidiary fractures to the inlet received more proppant than the farthest fractures. However, the propped area in the tertiary fracture slots was considerably less than in the primary and secondary ones. Two transport behaviors are found as the proppant flows into the secondary channel. Proppants roll down to the secondary channel by the gravity effect. Furthermore, Proppants were suspended in the secondary channel by vortices as the fluid velocity was high enough. Another channel is that straight channels have one or two-branched channels [19,26]. Particles mainly settled in the primary channel to form a high dune and were more likely to accumulate in the branched channel near the inlet. The turbulent flow and eddies at fracture intersections could decrease the particle dune height and improve particle transport deeper into narrow-branched fractures. [11,19,27–29].

Overall, previous literature studied proppant–fluid flow in planar fractures and complex fracture networks. Typically, curving fractures are the most common fracture in the reservoir due to the influence of formation heterogeneity and pre-existing fractures. Fracture shapes are more likely to be nonlinear. However, proppant placement characteristics in a curving fracture are still not well understood. Furthermore, there is no equation to quantitatively predict the coverage area of the proppant dune. For this reason, the present article's objective is to study the effect of curving fractures on proppant placement, particle size distribution, and particle dune area. Seven narrow channels with a curving section are set up to analyze proppant placement. A laser particle analyzer measures the particle size distributions in different positions of channels. Four dimensionless parameters are used to develop the relationship with the dune-covered area. A regression model is developed to calculate the percentage of covered area in curving fractures quantitively. It is beneficial to understand proppant placement and fracturing design.

2. Experimental System and Method

2.1. Experimental Method

Figure 1 shows the experimental system for proppant transport and placement in a curving channel. Natural sands are typically used as proppant in hydraulic fracturing [30], and four types of sands are used in the experiment, including 10/20 mesh, 20/40 mesh, 40/70 mesh, and 70/140 mesh. Table 1 lists the sand size and properties. Sands are mixed with tap water in the tank, and the sand flow rate is controlled by a funnel. A slurry pump with a variable frequency driver (VFD) is used to meet the requirements of the flow rates. To ensure accuracy, we calibrated the rate by collecting water at the outlet of the channel for a constant interval, then adjusted the rate by the VFD. During the experiment, the slurry is pumped into the channel by five holes on the channel inlet. Three cameras with 5472 × 3648 resolution record particle distribution. A 160-mesh sieve collected sands that flowed out of the channel at the outlet during the experiment. When the dune is equilibrium, the test is terminated. Once the test is complete and the channel is opened. Sand samples are collected from each individual region. Particle size distribution is measured by a laser particle analyzer.
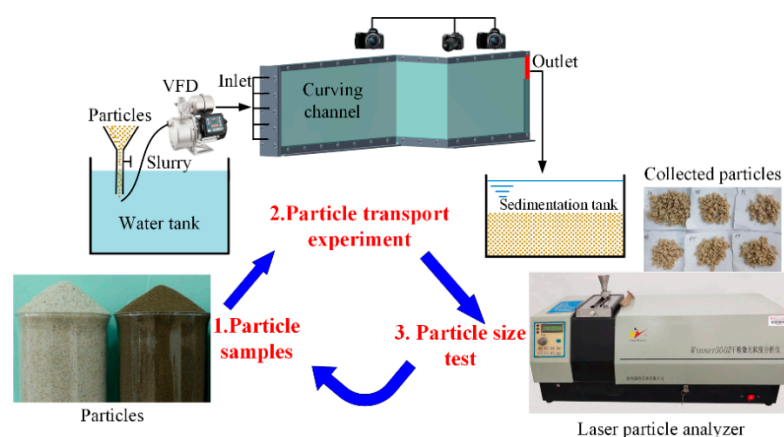

Figure 1. Experimental procedures and instruments.

Table 1. Particle parameters used in experiments.

Particle	Mesh	Size Range (mm)	Average Diameter d50 (mm)	Apparent Density ρ_p (kg/m^3)	Repose Angle θ_r (°)
Sand	10/20	2/0.84	1.41	2650	34.8
	20/40	0.84/0.42	0.633	2650	33.5
	40/70	0.42/0.212	0.311	2650	37.3
	70/140	0.212/0.053	0.155	2650	40.2

Figure 2 shows the structure and dimensions of a curving channel. To ensure the accuracy of the bending angle and the sealing at the bend, two whole acrylic sheets are bent twice at the required angle. A blue sticker is attached to one side of the channel as the background. The experimental channel is divided into three parts: the first straight section, the curving section, and the second straight section. The total length, height, and width are 1.5 m, 0.27 m, and 4 mm. Five injection holes are on the inlet boundary of the channel to simulate the perforation cluster; the hole diameter is 9 mm. The outlet is at the top right corner, which is similar to the channels [25,31]. The outlet height is 70 mm. The seven channels have the same inlet and outlet configuration to use the pumping system.

In Figure 2a, the bending angle varies from 45° to 180°, and other dimensions are kept constant. Four curving channels with varied bending angles are assembled. In Figure 2b, the bending angle is 90°, and the length of the first straight section varies from 0.25 m to 1.0 m. Correspondingly, the length of the second straight section changes from 1.0 m to 0.25 m. Four curving channels with varied distance ratios are used in the experiments.
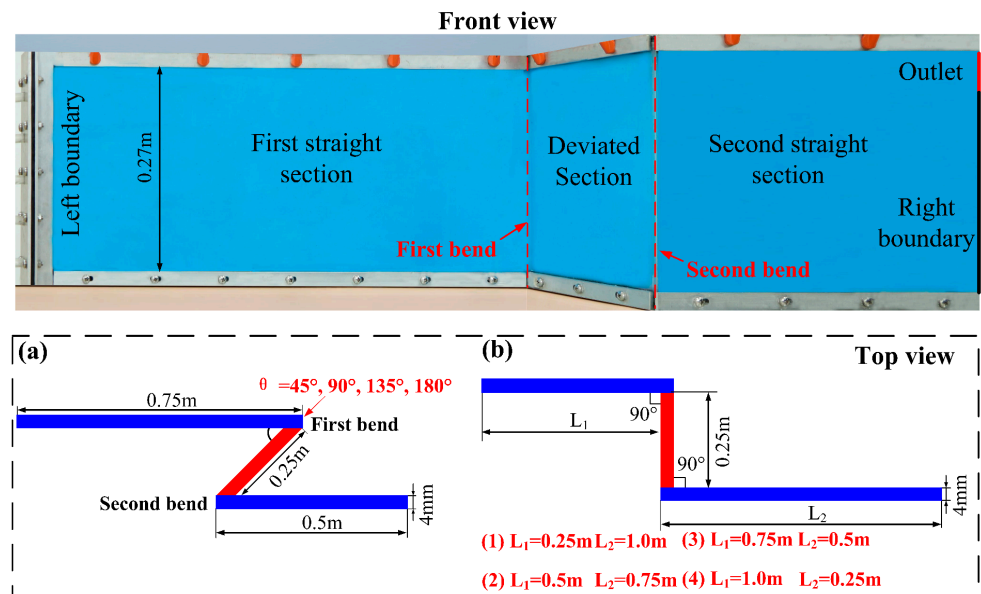
Front view

Figure 2. Curving channels at the front view and configurations at the top view.

Since the inner sizes of all channels are the same, 24 region codes from A1 to F4 are marked for describing the particle size and distribution, as shown in Figure 3.

Figure 3. The region codes of the channel for particle size analysis.

2.2. Sands and Fluid

Figure 4 shows four sizes of natural sands used in the present study, including 10/20 mesh, 20/40 mesh, 40/70 mesh, and 70/140 mesh. The size range is measured by the laser particle analyzer. The median-diameter d50 is a commonly used parameter to represent the average particle size [32]. It is defined as the particle size at which the cumulative volume percentage of particles reaches 50%. Table 1 lists the relevant physical properties of sands.
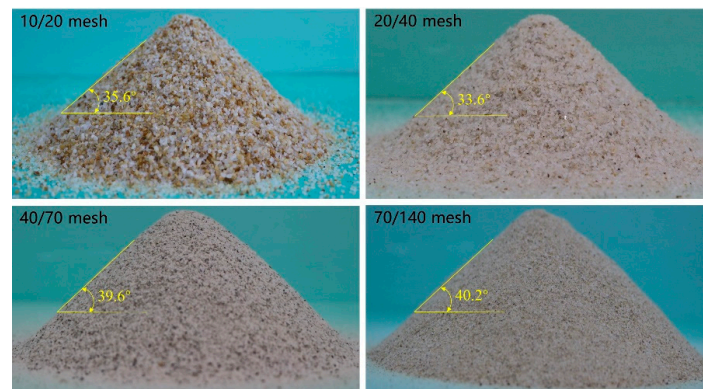

Figure 4. Particle samples used in experiments.

The sand mixes with tap water to prepare the slurry. The average slurry velocity in a fracture without proppant deposition typically ranges from 0.1 m/s to 0.5 m/s [25], the experimental velocity is from 0.12 m/s to 0.5 m/s.

2.3. Experimental Parameters

The percentage of the dune coverage area (*PCA*) can be used to evaluate particle placement, expressed by Equation (1).

$$PCA = \frac{PDA}{FCA} \times 100\% \tag{1}$$

where the *PDA* is the proppant dune area perpendicular to the width direction; *FCA* is the fracture cross-section area perpendicular to the width direction. The dimensionless numbers are typically used to set up the correlation for the fluid experiment [33]. The *PCA* has a relationship with the bending angle, the distance between the bending section and inlet, fluid velocity, and particle size. Thus, the dimensionless expression is as follows.

$$PCA = f\left(\theta, \frac{L_1}{L}, Re, S\right) \tag{2}$$

where θ is the bending angle; L_1 is the length of the first straight section; L is the total length of the channel; The Reynolds number of Re is expressed in Equation (3); The Shields number of S is expressed by Equation (5).

The Reynolds number Re is usually used to represent flow regimes, including turbulence and laminar flow.

$$Re = \frac{2\rho_f v_i l_h}{\mu_f} \tag{3}$$

where ρ_f is the fluid density, kg/m^3; μ_f is the fluid viscosity, Pa·s; v_i is the fluid velocity, m/s; l_h is the hydraulic diameter of the narrow channel.

$$l_h = \frac{2wh}{w+h} \tag{4}$$

where w is the channel width, m; h is the channel height, m.

Shields number represents the shear stress ratio at the dune top to the particle weight to analyze particle motion. At very low Shields Number, any settled proppant remains stationary and is hardly transported by fluid. Mack et al. [34] proposed the Shields number equation to represent particle transport in a narrow rectangular channel, expressed in Equation (5).

$$s = \frac{8v_i\mu_f}{(\rho_p - \rho_f)gd_pw} \tag{5}$$

where d_p is the mean particle diameter, m; ρ_g is particle density, kg/m^3; g is the gravitational acceleration, m/s^2.

Table 2 list the experimental parameters and dimensionless numbers. The *Re* is from 946 to 3942, and the *S* is from 0.04 to 0.32. Both parameters are in the typical range [35,36].

Table 2. Experimental parameters and dimensionless numbers.

Case	Fluid Phase	Particle Phase	Dimensionless Number			
	v_i (m/s)	d_{50} (mm)	L_1/L	θ (°)	Re	S
1	0.42	0.311	0.5	45/90/135/180	3311	0.16
2	0.42	0.311	0.16/0.33/0.5/0.66	90	3311	0.16
3	0.12	0.311	0.5	45/90/135/180	946	0.05
4	0.12	0.311	0.16/0.33/0.5/0.66	90	946	0.05

Table 2. *Cont.*

| Case | Fluid Phase | Particle Phase | Dimensionless Number | | | |
	v_i (m/s)	d_{50} (mm)	L_1/L	θ (°)	Re	S
5	0.21	0.311	0.5	45/90/135/180	1655	0.08
6	0.21	0.311	0.16/0.33/0.5/0.66	90	1655	0.08
7	0.5	0.311	0.5	45/90/135/180	3942	0.2
8	0.5	0.311	0.16/0.33/0.5/0.66	90	3942	0.2
9	0.42	0.155	0.5	45/90/135/180	3311	0.32
10	0.42	0.155	0.16/0.33/0.5/0.66	90	3311	0.32
11	0.42	0.633	0.5	45/90/135/180	3311	0.08
12	0.42	0.633	0.16/0.33/0.5/0.66	90	3311	0.08
13	0.42	1.41	0.5	45/90/135/180	3311	0.04
14	0.42	1.41	0.16/0.33/0.5/0.66	90	3311	0.04

3. Results and Analysis

3.1. Effect of the Angle, θ

Figure 5 shows four 40/70 mesh sand dunes at equilibrium for Case 1 (Table 2). For convenient comparison, three sections of the curving channel are placed in the plane. Two red dash lines in the figure mark the boundary of the curving section. The first straight section and the second straight section are located on the curving section's left and right sides. It should be noted that brown particles as a tracer agent are injected twice during the experiments for demarcating the dune into three regions, representing three injection sequences of S_1, S_2, and S_3. Figure 5a shows a sand dune in the straight channel. The region of S_1 shows the initial dune shape formed by the first injection sequence. The later injected sands are lifted to overshoot the front region of S1 and settle to the backside, forming the regions of S_2 and S_3 in sequence, which are identical to experimental results [14,25,37,38]. As the sand dune is in equilibrium, the dune height and shape are constant.
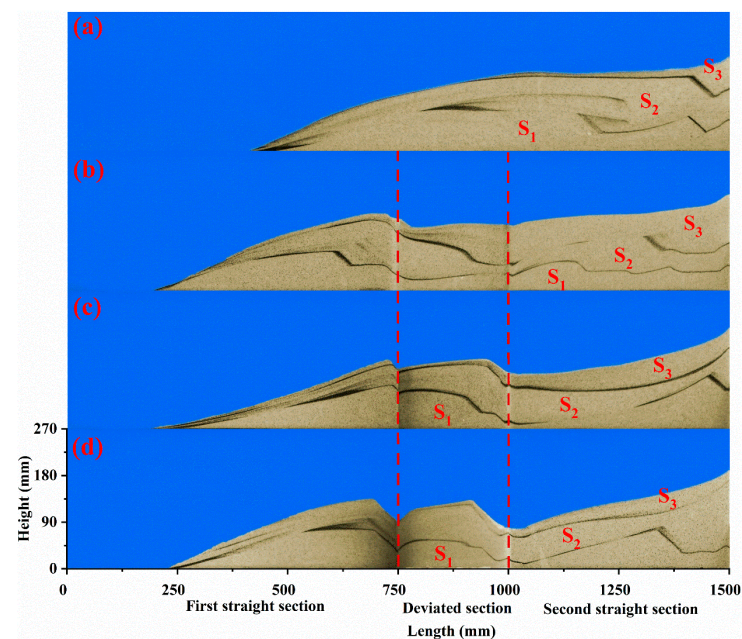

Figure 5. Snapshots of 40/70 mesh sand dunes in four channels at the stable status at L_1/L = 0.5, *Re* = 3311, and S = 0.16, front view: (**a**) The straight channel, θ = 180°; (**b**) The curving channel, θ = 135°; (**c**) The curving channel, θ = 90°; (**d**) The curving channel, θ = 45°.

The curving pathway significantly affects particle transport behaviors compared to the straight channel. More particles deposit in the first straight section and form a dune closer to the left boundary. It indicates that the curving section can hinder particle transport. The dune buildup in the curving section originates from two issues, as the following: (1) particle rolling from the first straight section; (2) particle settling in the suspension after colliding with the curving section. Although hindered by the curving section, many particles could be suspended through two bends and deposited along with the second straight section. Meanwhile, some particles directly flow out of the channel during the experiment. Another important finding is that the particle resuspension appears around two bends as the dune increase to a threshold value close to the equilibrium height, as shown in Figure 6. According to the observation, there are different scale vortices around the bends, and they are kept in the clockwise direction due to the turbulent stress [39]. The vortices can resuspend the settled particles through the curving section. Due to the vorticity around two bends, there are two depressions on the top of the dune.
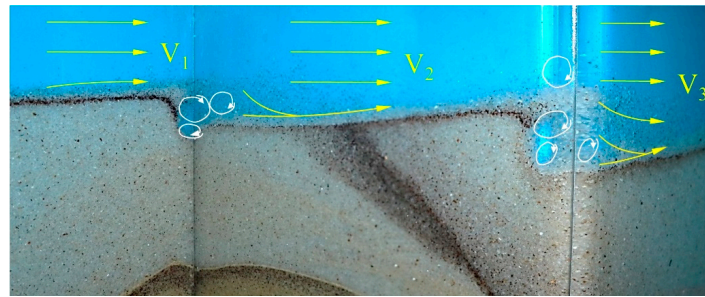

Figure 6. Vortices of 40/70 mesh sands around two bends, enlarged view of the deviated section in Figure 5c.

Once the test is complete and the channel is opened. Sand samples are collected from each individual region, illustrated in Figure 3. Particle size distribution is measured by a laser particle analyzer. Then, the contour map of the size distribution is obtained by the software of MATLAB 9.0, as shown in Figure 7. Particle sizes gradually reduce from the inlet to the outlet, and large particles accumulate in the front of the sand dune. In the straight channel, 65/70 mesh sands are in the E1 and F1 regions, and more than 70 mesh sands are in the F1. The result means small particles are easily transported deeper into the fracture during the first sequence of S_1. In the second last row from C2 to F2, they represent the second injection sequence of S_2, extensive sands sized from 40 to 60 mesh settle these regions. Furthermore, the particle size in the regions from D3 to F3 ranges from 40 to 50 mesh. Large sands deposit on the top of the dune at the late injection sequence, and smaller particles are out of the channel. The reason is that the decrease in the flow gap increases the fluid velocity, transporting larger particles out of the channel. As the bending angle decreases, it is founded that the mean particle sizes in E1 and F1 increase. For the angle of 45°, sand sizes range from 50 to 62 mesh in E1 and F1. It is interesting to note that there are more large sands in the straight section due to the curving section's hindrance. The particle size mainly ranges from 50 to 55 mesh in the curving section.

Four sand samples are collected at the outlet by a 160-mesh sieve when the injection time is 180 s. Figure 8a shows the particle size distributions of four collected samples. When the angle is 135°, the mean particle diameter of d_{50} is 303 μm, and the diameter increases to 317 μm at $\theta = 45°$, which is larger than the original mean diameter of 311 μm. For the straight channel, smaller sands ($d_{50} = 282$ μm) can flow out of the channel, and large particles deposit in the channel for the dune buildup, consistent with the experimental results [25,40]. In Figure 8b, it is found that the PCA decreases with the reduction of the bending angle. The PCA has a nonlinear correlation with the dimensionless number of angles. Fitting a natural logarithmic law trend through four data obtains a coefficient of determination, R^2 of 0.89.
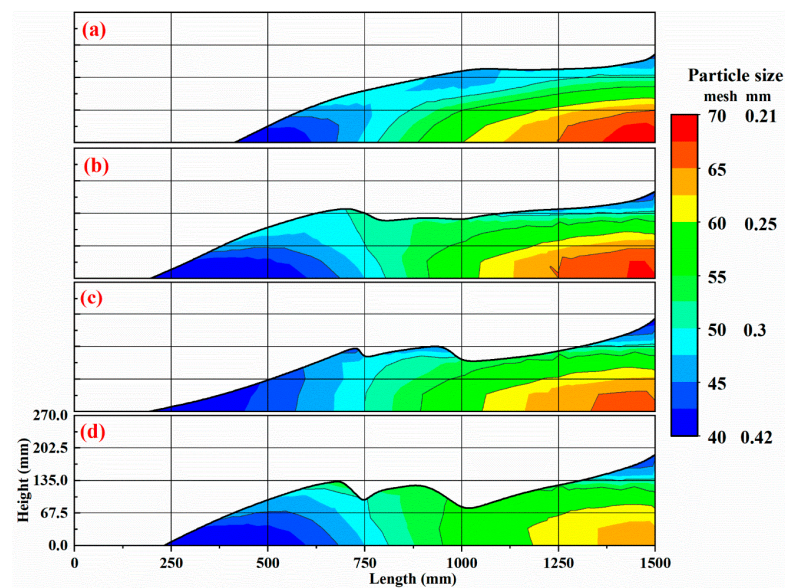
Figure 7. Mean particle size distribution across four channels: (**a**) The straight channel, $\theta = 180°$; (**b**) The curving channel, $\theta = 135°$; (**c**) The curving channel, $\theta = 90°$; (**d**) The curving channel, $\theta = 45°$.
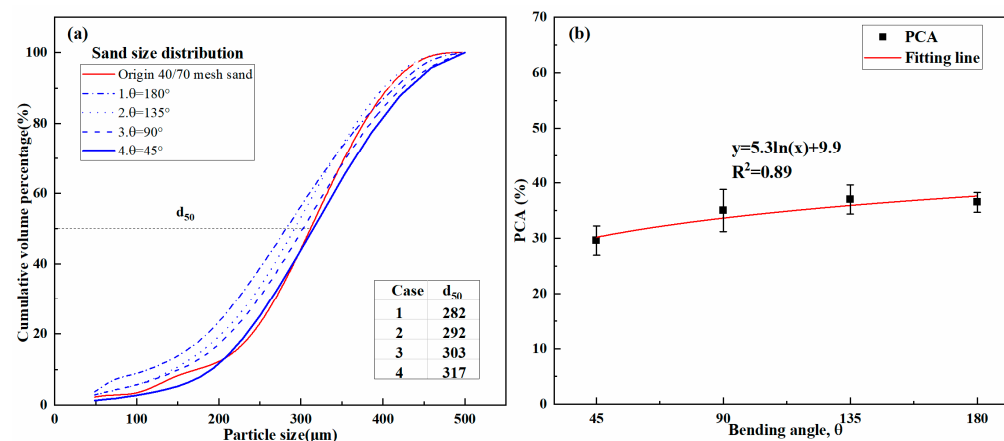

Figure 8. Effect of the bending angle on the particle dune distribution: (**a**) The particle size distributions of sands flowed out the channel at the injection time = 180 s; (**b**) The PCA in four channels with different bending angles.

In conclusion, as the bending angle decreases, a curving pathway induces fluid flow redirection and turbulent flow, enhancing particle transport capacity. As a result, more large particles are washed out of the channel. Moreover, the dune shape is more irregular and smaller.

3.2. Effect of the Distance Ratio, L_1/L

Since the location of the natural fracture is random, the distance between the natural fracture and the wellbore would be variable and affects the particle–fluid flow in the curving fracture. Figure 9 shows the 40/70 mesh sand dunes in four channels for Case 2 (Table 2). Two red dash lines in the figure mark the boundary of the curving section. It should be noted that brown particles as a tracer agent are injected twice during the experiments for demarcating the dune into three regions, representing three injection sequences of S_1, S_2, and S_3. In Figure 9a,b, there is a large depleted zone without sands between the left boundary and the front side of the particle dune. In Figure 9a, almost all sands are transported through the curving section and deposited in the second straight section. However, the fracture will close in the depleted zone because there are no proppants to prop the fracture, and the closure region will significantly increase flow friction during

production. According to the size of the depleted zone, it is found that the curving section has a hindering effect on particle transport as the ratio increases. As the ratio is more than 0.33, the dune's front side is closer to the inlet, and more sands deposit in the first straight section.
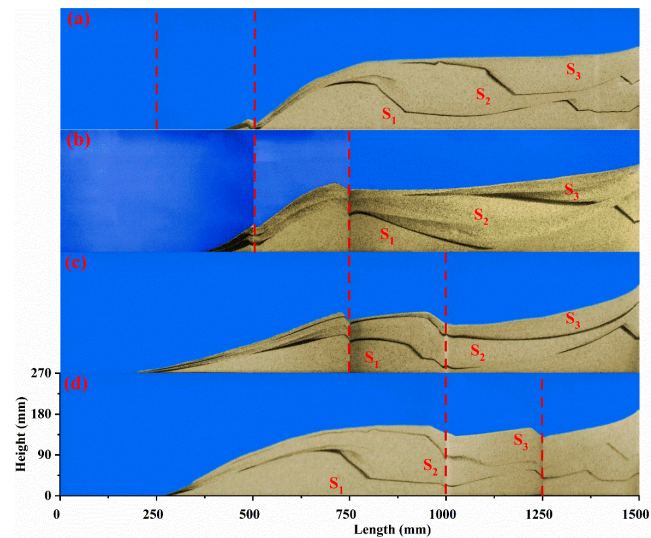

Figure 9. Snapshots of 40/70 mesh sand dunes in four channels at equilibrium at $\theta = 90°$, *Re* = 3311 and S = 0.16, front view: (**a**) L_1/L = 0.16; (**b**) L_1/L = 0.33; (**c**) L_1/L = 0.5; (**d**) L_1/L = 0.66.

Figure 10 shows the contour map of the particle size distribution in four channels with different distance ratios. In Figure 10a, the particle size distribution in the second straight section is similar to that in the straight channel. After the injected particle flows through the curving section, large particles settle in the front, and the small particles deposit in the end. For the late injected sequences of S_2 and S_3, more large particles build up the dune in the channel. As the distance ratio increases, the curving section is far away from the entrance, and more large particles sized from 40 to 50 mesh are hindered in the first straight section. Furthermore, the smaller particles hardly deposit at the end of the channel. For example, Figure 10d shows that the sand size in the F1 is from 60 to 65 mesh. The probable explanation is that the vortex flow around two bends is closer to the outlet, so smaller particles are prone to flow out of the channel by the vortex.
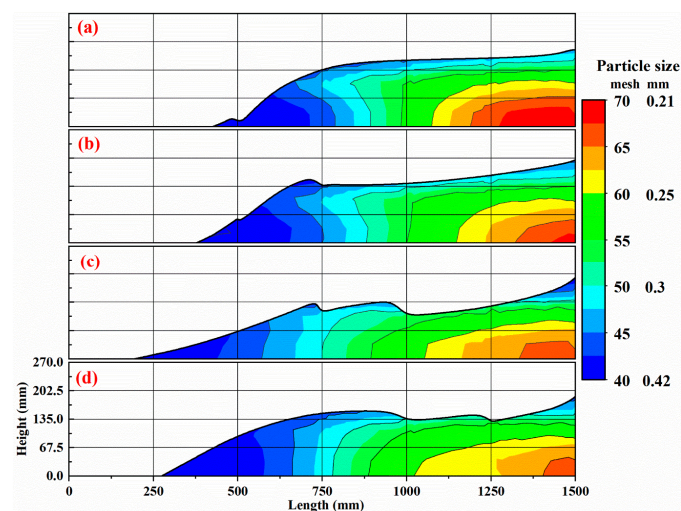

Figure 10. Mean particle size distribution across four channels: (**a**) L_1/L = 0.16; (**b**) L_1/L = 0.33; (**c**) L_1/L = 0.5; (**d**) L_1/L = 0.66.

Figure 11a shows the particle size distributions for the sand deposited in the sedimentation tank when the injection time is 180 s. Compared to the original distribution, the bigger particle could flow out of the channel with a smaller distance ratio. When the ratio is 0.166, the mean diameter is 316 μm. When the ratio increases to 0.66, the diameter decreases to 291 μm. Figure 11b shows a natural logarithmic law trend between the PCA and distance ratio.
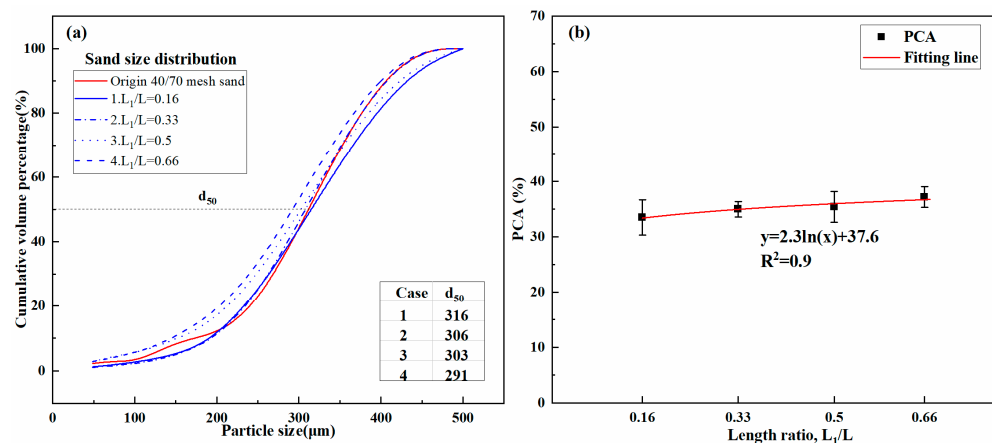

Figure 11. Effect of the distance ratio on the particle dune distribution: (**a**) The particle size distributions of sands flowed out the channel at the injection time = 180 s; (**b**) The PCA in four channels with different distance ratios.

3.3. Effect of the Reynolds Number, Re

Since the particle transport originated from the fluid flow, the flow pattern would affect the particle distribution. Figure 12 shows the front view of 40/70 mesh sand distributions in four channels for Case 3 (Table 2), the slurry flow shown in Figure 12 is laminar. Two red dash lines in the figure mark the boundary of the curving section. The 40/70 mesh sand builds up a higher dune in the straight channel, closer to the left boundary. For the curving channel, three dunes contact the entrance. In Figure 12c,d, the lowest injection hole was totally blocked during the experiment. The curving pathway has a more hindering effect on particle deposition in laminar flow with a low Reynolds number, especially in the channel with small bending angles. The flow would change to turbulence when the dune increases to a threshold height, and then the vortex flow appears around two bends. Due to the vortex wash, depression will be formed around the bend. The smaller the bending angle, the larger the depression.

Figure 13 shows the front view of 40/70 mesh sand distributions in four channels for Case 4 (Table 2). It is found that the distance ratio has little effect on particle distribution when the flow is laminar. Particle settlement and bedload dominate the transport mechanisms [37]. As a result, the injected particles quickly settle near the entrance and accumulate a high dune in the channel.

In Figure 14, Re has a negative linear correlation with PCA. The experiments are Cases 1 to 8. The higher the Reynolds number, the lower the covered areas, especially in the curving channel. When the Re is 3942, the flow is turbulent, and the PCA significantly decreases. The minimum value is 17.2% in the channel with 45° bends. The linear fitting model has a good correlation between PCA and Re, and R^2 values range from 0.96 to 0.98. These trends indicate that the smaller bending angle has more effect on particle deposition than the straight channel.
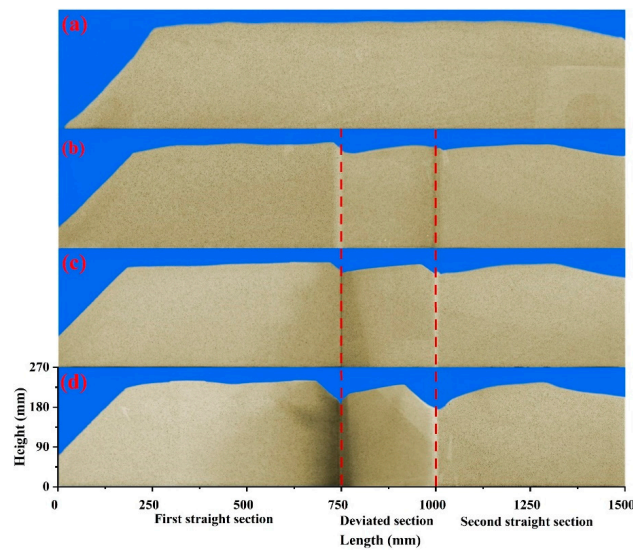
Figure 12. Snapshots of 40/70 mesh sand dunes in four channels at the stable status at Re = 946, S = 0.05, and L_1/L = 0.5, front view: (**a**) The straight channel, θ = 180°; (**b**) The curving channel, θ = 135°; (**c**) The curving channel, θ = 90°; (**d**) The curving channel, θ = 45°.
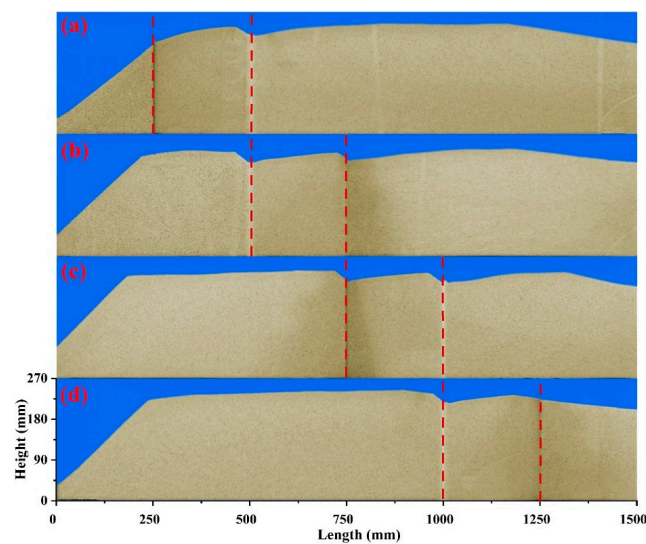

Figure 13. Snapshots of 40/70 mesh sand dunes in four channels at the stable status at Re = 946, S = 0.05 and θ = 90°, front view: (**a**) L_1/L = 0.16; (**b**) L_1/L = 0.33; (**c**) L_1/L = 0.5; (**d**) L_1/L = 0.66.
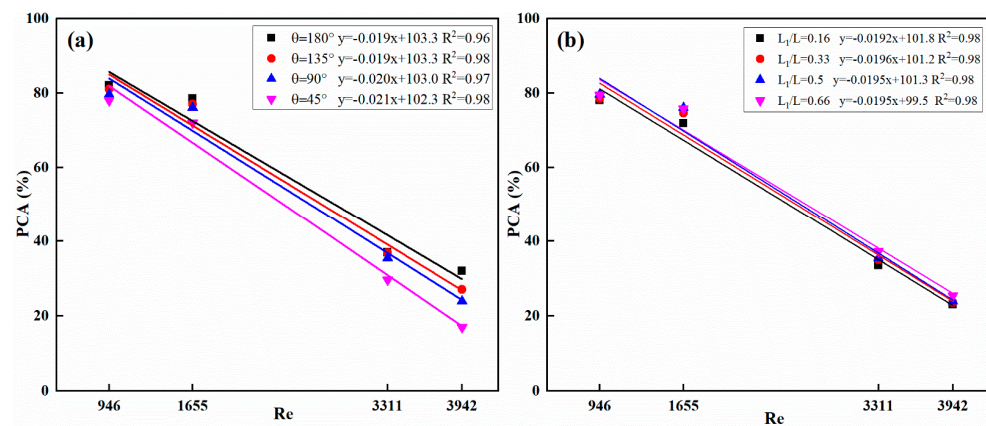

Figure 14. The correlations between Re and PCA: (**a**) The bending angle; (**b**) The distance ratio.

3.4. Effect of the Shields Number, S

The Shields number has a substantial impact on the particle placement in different channels. In Figure 15, two red dash lines in the figure mark the boundary of the curving section. In Figure 15a, a lot of sand is deposited in the straight channel to form a large dune. As the sand is transported in the curving channel with the angle of 135°, more sands flow out of the channel, and the dune area decreases, as shown in Figure 15b. In Figure 15d, the injected 70/140 mesh sands mainly deposit in the second straight section, and a few particles deposit in the curving section. The probable reason is that the curving channel with small bending angles induces turbulent flow, transporting more smaller particles out of the channel.
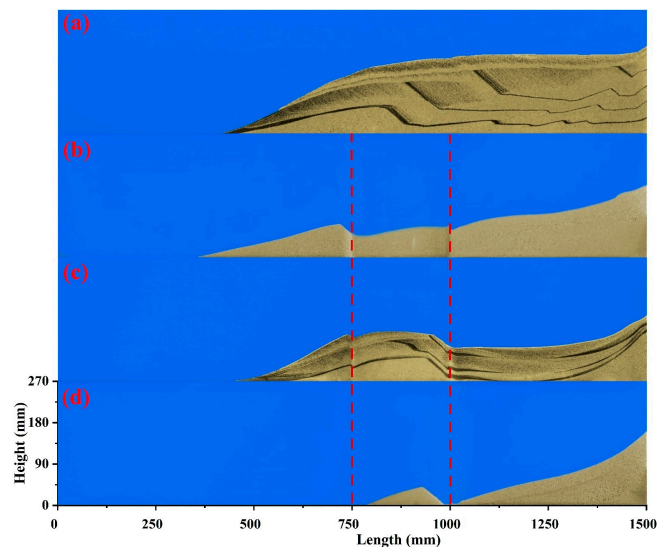

Figure 15. Snapshots of 70/140 mesh sand dunes in four channels at the stable status at Re = 3311 and L_1/L = 0.5, front view: (**a**) The straight channel, θ = 180°; (**b**) The curving channel, θ = 135°; (**c**) The curving channel, θ = 90°; (**d**) The curving channel, θ = 45°.

Figure 16 shows the front view of 70/140 mesh sand distributions in four channels for Case 10 (Table 2). When the ratio is 0.16, sands build up a dune in the second straight section, far away from the second bends. As the ratio increases to 0.66, particles build up a dune closer to the entrance due to the hindering effect, as shown in Figure 16d.
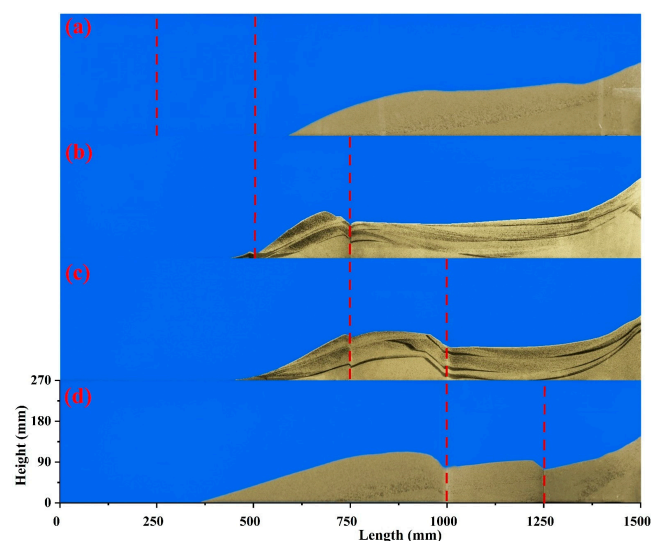

Figure 16. Snapshots of 70/140 mesh sand dunes in four channels at the stable status at *Re* = 3311 and θ = 90°, front view: (**a**) L_1/L = 0.16; (**b**) L_1/L = 0.33; (**c**) L_1/L = 0.5; (**d**) L_1/L = 0.66.

Figure 17 shows that the S has a negative linear correlation with PCA. The experiments are Cases 1 to 2 and Cases 9 to 14. The larger the Shields number, the lower the area of the dune. The minimum value is 8.5% in the channel with 45° bends. The linear fitting model has a good correlation between PCA and S, and R^2 values range from 0.87 to 0.98. Thus, it can conclude that the smaller particles smoothly flow through the curving section deeper into the channel. For the complex fracture system, the small particle is recommended for propping the remote fracture region.
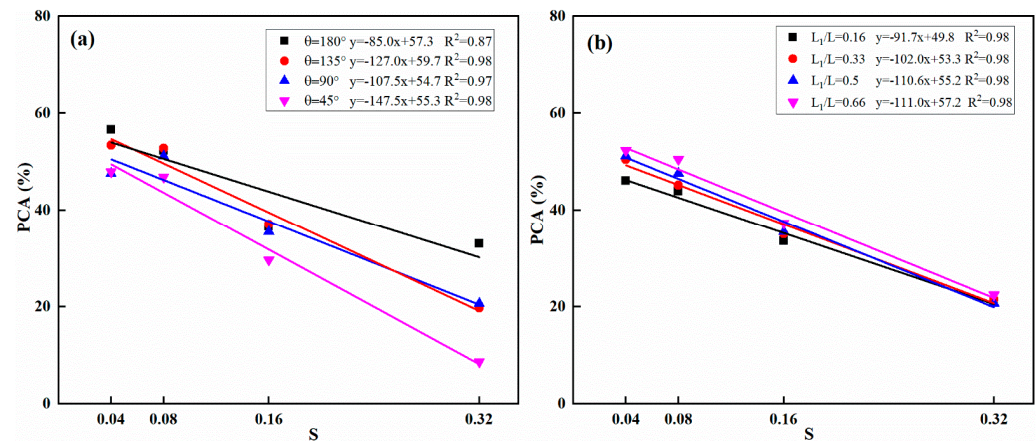

Figure 17. The correlations between S and *PCA*: (**a**) The bending angle; (**b**) The distance ratio.

4. Discussion

It is found that the *PCA* has relationships with four factors. According to the 56 experimental data, the correlation between the *PCA* and dimensionless parameters is modeled by the multivariable linear regression method, as shown in Equation (6).

$$PCA = 78.6 - 109.2S - 0.014Re + \ln\left(\theta^{5.5}\left(\frac{L_1}{L}\right)^{2.3}\right) \ R^2 = 0.98 \tag{6}$$

To evaluate the accuracy and reliability of developed models, the absolute percentage error (*APE*), mean absolute percentage error (*MAPE*), relative percentage error (*RPE*), and mean relative percentage error (*MRPE*) are used as follows:

$$APE = \left|\frac{E_i - P_i}{E_i}\right| \times 100\% \tag{7}$$

$$MAPE = \frac{1}{n}\sum_{i=1}^{n}\left|\frac{E_i - P_i}{E_i}\right| \times 100\% \tag{8}$$

$$RPE = |E_i - P_i| \times 100\% \tag{9}$$

$$MRPE = \frac{1}{n}\sum_{i=1}^{n}|E_i - P_i| \times 100\% \tag{10}$$

where E_i is the experimental result; P_i is the prediction value; n is the sample number.

Figure 18 shows the errors. In Figure 18a, *MRPE* is 2.77%, and the maximum *RPE* is 5.56%. In Figure 18b, *MAPE* is 6.34% for all experimental results, and the *APE* is 12.9%. The small errors mean the regression model can reliably predict the covered area of the particle dune in curved fractures.
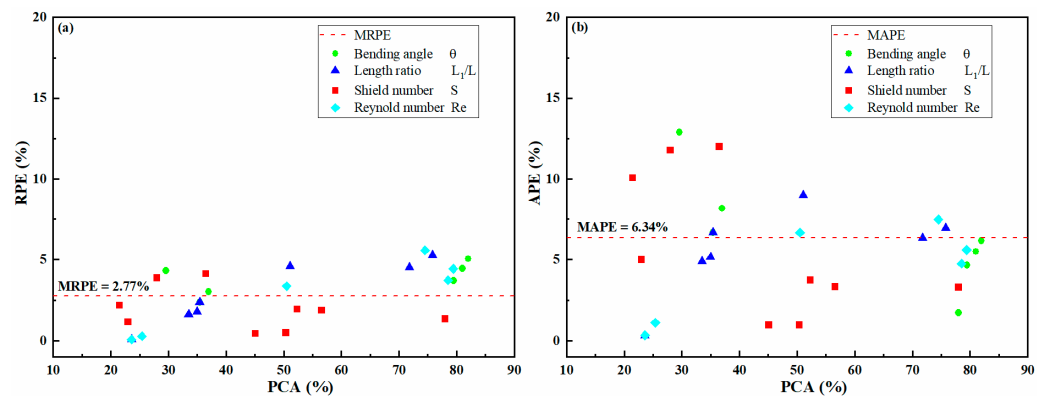
Figure 18. Error analysis. (**a**) Relative error; (**b**) Absolute error.

5. Conclusions

This work conducted a proppant transport experiment to reveal the particle placement characteristics in complex curving fractures. The effects of the fracture angle, the distance between the curving section and inlet, fluid velocity, and particle size on proppant placement were studied. Furthermore, the particle size distribution and proppant dune area were analyzed. Then, the primary conclusions are obtained as follows.

1. Due to the influence of the curving section, the liquid flow direction changes twice, leading to a change in particle settling behavior. The uneven deposition along the whole channel causes an irregular proppant dune. The large sand is prone to deposit at the front side of the dune, and small particles can move deeper into the curving fracture.
2. The curving section has a hindering effect on sand placement. The dune in the curving fracture is closer to the inlet compared to the straight fracture. With the decrease in the bending angle, more large particles would be transported out of the channel, and a lower and smaller dune is built up in the fracture.
3. As the curving section is farther away from the inlet, particles deposit near the inlet and form a larger proppant dune. In contrast, more particles flow through the curving section and deeper into the fracture. A large depleted zone is formed in the first and curving sections, significantly decreasing the fracture conductivity.
4. The Reynolds number and Shields number can significantly affect particle–fluid flow in curving fractures. The increase in Reynolds number and Shields number would significantly improve particle transport capacity, leading to the reduction of the covered area of the particle dune.
5. The proposed model, including four factors, can quantitatively predict the covered area of the proppant dune in curving fractures. The minor errors mean the high reliability of the equation.

Author Contributions: Conceptualization, Z.W.; methodology and formal analysis C.W.; writing—original draft preparation, L.Z. All authors have read and agreed to the published version of the manuscript.

Institutional Review Board Statement: Not applicable.

Informed Consent Statement: Not applicable.

Data Availability Statement: The data that support the findings of this study are available from the corresponding author upon reasonable request.

Conflicts of Interest: The authors declare no conflict of interest.

References

1. Qu, H.; Tang, S.; Sheng, M.; Liu, Z.; Wang, R.; Hu, Y. Experimental investigation of the damage characteristics and breaking process of shale by abrasive waterjet impact. *J. Pet. Sci. Eng.* **2022**, *211*, 110165. [CrossRef]
2. Qu, H.; Tang, S.; Liu, Z.; McLennan, J.; Wang, R. Experimental investigation of proppant particles transport in a tortuous fracture. *Powder Technol.* **2021**, *382*, 95–106. [CrossRef]
3. Li, J.; Liu, P.; Kuang, S.; Yu, A. Visual lab tests: Proppant transportation in a 3D printed vertical hydraulic fracture with two-sided rough surfaces. *J. Pet. Sci. Eng.* **2021**, *196*, 107738. [CrossRef]
4. Qu, H.; Wang, R.; Ao, X.; Xue, L.; Liu, Z.; Lin, H. The Investigation of Proppant Particle-Fluid Flow in the Vertical Fracture with a Contracted Aperture. *SPE J.* **2022**, *27*, 274–291. [CrossRef]
5. Qu, H.; Liu, Y.; Zeng, S.; Xiao, H.; Lu, Y.; Liu, Z. Effect of Natural Fracture Characteristics on Proppant Transport and Placement in an Irregular, Nonplanar Fracture. *SPE J.* **2022**, *27*, 2208–2225. [CrossRef]
6. Warpinski, N.R.; Teufel, L.W. Influence of Geologic Discontinuities on Hydraulic Fracture Propagation (includes associated papers 17011 and 17074). *J. Pet. Technol.* **1987**, *39*, 209–220. [CrossRef]
7. Lee, H.; Olson, J.; Holder, J.; Gale, J.; Myers, R. The interaction of propagating opening mode fractures with preexisting discontinuities in shale: Shale vein-fracture interaction. *J. Geophys. Res. Solid Earth* **2014**, *120*, 169–181. [CrossRef]
8. Fu, W.; Savitski, A.A.; Damjanac, B.; Bunger, A.P. Three-dimensional lattice simulation of hydraulic fracture interaction with natural fractures. *Comput. Geotech.* **2019**, *107*, 214–234. [CrossRef]
9. Wu, X.; Huang, Z.; Cheng, Z.; Zhang, S.; Song, H.; Zhao, X. Effects of cyclic heating and LN2-cooling on the physical and mechanical properties of granite. *Appl. Therm. Eng.* **2019**, *156*, 99–110. [CrossRef]
10. Wu, X.; Huang, Z.; Zhang, S.; Cheng, Z.; Li, R.; Song, H.; Wen, H.; Huang, P. Damage Analysis of High-Temperature Rocks Subjected to LN2 Thermal Shock. *Rock Mech. Rock Eng.* **2019**, *52*, 2585–2603. [CrossRef]
11. Liou, T.-M.; Tzeng, Y.-Y.; Chen, C.-C. Fluid Flow in a 180 deg Sharp Turning Duct with Different Divider Thicknesses. *J. Turbomach.* **1999**, *121*, 569–576. [CrossRef]
12. Zhang, Y.; Chai, J. Effect of surface morphology on fluid flow in rough fractures: A review. *J. Nat. Gas Sci. Eng.* **2020**, *79*, 103343. [CrossRef]
13. Sahai, R.; Moghanloo, R.G. Proppant transport in complex fracture networks—A review. *J. Pet. Sci. Eng.* **2019**, *182*, 106199. [CrossRef]
14. Kern, L.; Perkins, T.; Wyant, R. The mechanics of sand movement in fracturing. *J. Pet. Technol.* **1959**, *11*, 55–57. [CrossRef]
15. Babcock, R.; Prokop, C.; Kehle, R. Distribution of propping agent in vertical fractures. In *Drilling and Production Practice*; American Petroleum Institute: New York, NY, USA, 1967.
16. Wang, J.; Joseph, D.D.; Patankar, N.A.; Conway, M.; Barree, R.D. Bi-power law correlations for sediment transport in pressure driven channel flows. *Int. J. Multiph. Flow* **2003**, *29*, 475–494. [CrossRef]
17. Woodworth, T.R.; Miskimins, J.L. Extrapolation of Laboratory Proppant Placement Behavior to the Field in Slickwater Fracturing Applications. In Proceedings of the SPE Hydraulic Fracturing Technology Conference, College Station, TX, USA, 29–31 January 2007; Society of Petroleum Engineers: College Station, TX, USA, 2007; p. 12.
18. Hu, X.; Wu, K.; Li, G.; Tang, J.; Shen, Z. Effect of proppant addition schedule on the proppant distribution in a straight fracture for slickwater treatment. *J. Pet. Sci. Eng.* **2018**, *167*, 110–119. [CrossRef]
19. Tong, S.; Mohanty, K.K. Proppant transport study in fractures with intersections. *Fuel* **2016**, *181*, 463–477. [CrossRef]
20. Fjaestad, D.; Tomac, I. Experimental investigation of sand proppant particles flow and transport regimes through narrow slots. *Powder Technol.* **2019**, *343*, 495–511. [CrossRef]
21. Zeng, H.; Jin, Y.; Qu, H.; Lu, Y.-H. Experimental investigation and correlations for proppant distribution in narrow fractures of deep shale gas reservoirs. *Pet. Sci.* **2021**, *19*, 619–628. [CrossRef]
22. Tong, S.; Singh, R.; Mohanty, K.K. A visualization study of proppant transport in foam fracturing fluids. *J. Nat. Gas Sci. Eng.* **2018**, *52*, 235–247. [CrossRef]
23. Hou, L.; Sun, B.; Wang, Z.; Li, Q. Experimental study of particle settling in supercritical carbon dioxide. *J. Supercrit. Fluids* **2015**, *100*, 121–128. [CrossRef]
24. Wen, Q.; Wang, S.; Duan, X.; Li, Y.; Wang, F.; Jin, X. Experimental investigation of proppant settling in complex hydraulic-natural fracture system in shale reservoirs. *J. Nat. Gas Sci. Eng.* **2016**, *33*, 70–80. [CrossRef]
25. Sahai, R.; Miskimins, J.L.; Olson, K.E. Laboratory Results of Proppant Transport in Complex Fracture Systems. In Proceedings of the SPE Hydraulic Fracturing Technology Conference, The Woodlands, TX, USA, 4–6 February 2014; Society of Petroleum Engineers: The Woodlands, TX, USA, 2014; p. 26.
26. Li, N.Y.; Li, J.; Zhao, L.Q.; Luo, Z.F.; Liu, P.L.; Guo, Y.J. Laboratory Testing on Proppant Transport in Complex-Fracture Systems. *SPE Prod. Oper.* **2017**, *32*, 382–391. [CrossRef]
27. Fan, L.F.; Wang, H.D.; Wu, Z.J.; Zhao, S.H. Effects of angle patterns at fracture intersections on fluid flow nonlinearity and outlet flow rate distribution at high Reynolds numbers. *Int. J. Rock Mech. Min. Sci.* **2019**, *124*, 104136. [CrossRef]
28. Wang, X.; Yao, J.; Gong, L.; Sun, H.; Liu, W. Numerical simulations of proppant deposition and transport characteristics in hydraulic fractures and fracture networks. *J. Pet. Sci. Eng.* **2019**, *183*, 106401. [CrossRef]
29. Yue, M.; Zhang, Q.; Zhu, W.; Zhang, L.; Song, H.; Li, J. Effects of proppant distribution in fracture networks on horizontal well performance. *J. Pet. Sci. Eng.* **2020**, *187*, 106816. [CrossRef]

30. Miskimins, J. *Hydraulic Fracturing: Fundamentals and Advancements*; Society of Petroleum Engineers: Danbury, CT, USA, 2020.
31. Fernández, M.E.; Sánchez, M.; Pugnaloni, L.A. Proppant transport in a scaled vertical planar fracture: Vorticity and dune placement. *J. Pet. Sci. Eng.* **2019**, *173*, 1382–1389. [CrossRef]
32. Chhabra, R.P. *Bubbles, Drops, and Particles in Non-Newtonian Fluids*, 2nd ed.; CRC Press: Boca Raton, FL, USA, 2007.
33. Zohuri, B. *Dimensional Analysis and Self-Similarity Methods for Engineers and Scientists*; Springer: Berlin/Heidelberg, Germany, 2015.
34. Mack, M.; Sun, J.; Khadilkar, C. Quantifying Proppant Transport in Thin Fluids: Theory and Experiments. In Proceedings of the SPE Hydraulic Fracturing Technology Conference, The Woodlands, TX, USA, 4–6 February 2014; Society of Petroleum Engineers: The Woodlands, TX, USA, 2014; p. 14.
35. Morsi, S.A.; Alexander, A.J. An investigation of particle trajectories in two-phase flow systems. *J. Fluid Mech.* **1972**, *55*, 193–208. [CrossRef]
36. Miller, M.C.; McCave, I.N.; Komar, P.D. Threshold of sediment motion under unidirectional currents. *Sedimentology* **1977**, *24*, 507–527. [CrossRef]
37. McClure, M. Bed load proppant transport during slickwater hydraulic fracturing: Insights from comparisons between published laboratory data and correlations for sediment and pipeline slurry transport. *J. Pet. Sci. Eng.* **2018**, *161*, 599–610. [CrossRef]
38. Liu, Y. Settling and Hydrodynamic Retardation of Proppants in Hydraulic Fractures. Ph.D. Thesis, University of Texas at Austin, Austin, TX, USA, 2006.
39. Joseph, H.; Spurk, N.A. *Fluid Mechanics*; Springer: Berlin/Heidelberg, Germany, 2020.
40. Anschutz, D.A.; Lowrey, T.A.; Stribling, M.; Wildt, P.J. An In-Depth Study of Proppant Transport and Placement with Various Fracturing Fluids. In Proceedings of the SPE Annual Technical Conference and Exhibition, Calgary, AB, Canada, 30 September–2 October 2019; Society of Petroleum Engineers: Calgary, AB, Canada, 2019; p. 27.